J. Appl. Comput. Mech., 12(1) (2026) 238-254
DOI: 10.22055/jacm.2025.48275.5112

ISSN: 2383-4536
jacm.scu.ac.ir

Shahid Chamran University of Ahvaz

Journal of Applied and Computational Mechanics

Research Paper

Numerical Analysis of Two Side-by-Side Flexible Filaments in Shear Flow and Orbit Class Prediction using Immersed Boundary Method and Machine Learning Techniques

Mithun Kanchan[1], Ranjith Maniyeri[2], Omkar S. Powar[3]

[1] Department of Mechanical and Industrial Engineering, Manipal Institute of Technology, Manipal Academy of Higher Education, Manipal-576104, Karnataka, India, Email: mithun.kanchan@manipal.edu

[2] Biophysics Lab, Department of Mechanical Engineering, National Institute of Technology Karnataka, Surathkal, Mangalore-575025, India, Email: mranji1@nitk.edu.in

[3] Department of Biomedical Engineering, Manipal Institute of Technology, Manipal Academy of Higher Education, Manipal-576104, Karnataka, India, Email: omkar.powar@manipal.edu

Received March 02 2025; Revised May 27 2025; Accepted for publication May 27 2025.
Corresponding author: O.S. Powar (omkar.powar@manipal.edu)

Abstract. This study utilizes a second-order immersed boundary method (IBM) for investigating the orbital dynamics of two flexible, inextensible filaments placed side-by-side in low-Reynolds-number shear flows. A parametric analysis explores the effects of filament length, bending rigidity, and shear-strain rate on filament deformation and interaction. The dynamic behavior of the filaments is characterized by a flow-filament offset ratio (φ). Results reveal that at high shear rates and filament lengths, the first filament (F1) minimally influences the hydrodynamic forces acting on the second filament (F2), leading to independent deformation patterns. However, at moderate lengths (L ≈ 0.2) and high shear rates (G ≈ 32), F1 significantly impacts F2 deformation. Spectrogram analyses show that F1 absorbs fluid forces, generating multiple energy bands, while F2 experiences reduced forces, resulting in retarded motion and larger band gaps. A predictive model based on simulation results is developed using five machine learning classifiers: Naïve Bayes, Support Vector Machine (SVM), K-Nearest Neighbor (KNN), Decision Tree, and Artificial Neural Network (ANN). Among these, KNN prediction for F2 outperforms, achieving an Accuracy of 0.889, Precision of 0.878, Recall of 0.875, F1 Score of 0.875, and ROC Area of 0.929, making it the most effective method for classifying filament orbital regimes. The findings of this study will pave the way for the next generation of microfluidic devices, unlocking unprecedented possibilities in particle sorting through the innovative use of flexible filaments.

Keywords: Flexible filament, Fluid-structure interaction, Immersed boundary method, Low Reynolds number, Machine Learning.

1. Introduction

In the past few years, extensive research has been carried to understand and model complex mechanical deformations of thin, in-extensible flexible filament due to its relevance in various biotechnological applications such as diatom chains [1], DNA synthesis [2], proteins and polymers [3, 4] etc. The dynamic interplay between structural resistance offered by the flexible filament and hydrodynamics forces generated by incompressible, viscous shear flow surrounding the filament is a challenging Fluid-Structure Interaction (FSI) problem that needs to be addressed in order to better understand the mechanical behavior underlying such an overall system.

This Investigations to study the response of flexible filaments in viscous shear flow were carried out experimentally, numerically and theoretically. The dynamics of neutrally buoyant, rigid spheroid particles in Couette flow was studied by Jeffrey [5]. The motion can be described using Jeffrey's equation given in Eq. (1):

$$\alpha(t) = \tan^{-1}\left(r_e \tan\left(\frac{K r_e t}{r_e^2 + 1}\right)\right) \tag{1}$$

where, $\alpha(t)$ is the angle made by the rigid particle, K is the rate of shear and r_e is the particle aspect ratio. The above equation can also be used to describe motion of rigid, cylindrical filaments in place of ellipsoids, by modifying the aspect ratio r_e [6]. The vibrant range of motions exhibited by flexible filaments when subjected to shear flow was experimentally analyzed by Forgacs and Mason [7]. They observed that the factors that largely effect the filament deformation were shear rate (G), bending rigidity (K_b) and filament length (L). Several techniques were developed to simulate the dynamical behavior of rigid and flexible filaments in flow. Some important studies include Yamamoto and Matsuoka [8], Ross and Klingenberg [9], Shelley and Ueda [10], Tornberg and Shelley [11], Jendrejack et al. [12], Lindström and Uesaka [13, 14], Bouzarth et al. [15], Słowicka et al. [16] etc. Recently, Immersed Boundary Method

Published online: May 30 2025

(IBM) developed by Peskin [17] has emerged as a powerful simulation tool to study and analyze the dynamics of rigid and flexible filaments in viscous fluid flow especially low Reynolds number flows. Stockie and Green [18], performed two-dimensional numerical simulation of wood pulp fiber using IBM and categorized fiber deformation into various orbit classes such as Rigid, Springy, C-shape, Complex shapes etc. They also extended their study to carry out three-dimensional simulation of the fibers in shear flow. The recreation of two-dimensional flexible filament orbit classes utilizing modified versions of IBM were successfully carried out by Weins and Stockie [19] and Kanchan and Maniyeri [20]. However, due to the restricted time-step and stability issues, the numerical simulation of FSI problems is computationally expensive. There is a need to obtain filament deformation and observe the surrounding fluid motion accurately in two-dimensional regime, by using less computational resources and reducing mesh generation overheads. This can be achieved by combining numerical simulation of IBM with predictive capabilities of machine learning algorithms.

In recent years, the use of machine learning algorithms has gained significant importance, especially in engineering applications. In comparison to numerical methods, machine learning algorithms can solve complex mathematical problems at reduced computational cost and results are found to be reliable. A critical factor influencing the feasibility and reliability of machine learning (ML) models in such studies is the training pipeline. This process typically involves multiple stages, including data preprocessing, feature selection, model training, and evaluation. Effective preprocessing is essential for eliminating noise and inconsistencies, ensuring that the input data accurately reflects the underlying physical phenomena. Feature selection plays a crucial role in identifying the most informative parameters, such as filament length, bending rigidity, and shear rate, which are essential for capturing the system's dynamic behavior. Model training then leverages this refined data to uncover intricate relationships and patterns within the dataset. Finally, evaluation metrics like precision, recall, and overall accuracy are used to assess the model's performance and generalization capability, particularly when dealing with complex, nonlinear, and high-dimensional datasets typical in fluid-structure interaction studies. These steps collectively contribute to building robust, interpretable, and physically meaningful ML models.

Convolution Neural Networks (CNN) were employed by Miyanawala and Jaiman [21] to solve unsteady FSI problem by developing a hybrid data-driven network. In order to study the movement of sperm and perform sorting, Koh et al. [22] used supervised learning techniques. The frequency of flaps when a 2-D flexible filament is placed in soap-film was studied using Artificial Neural Network (ANN) by Fayed et al. [23]. The effects on the dynamics of two side-by-side flexible filaments subjected to shear flow and prediction of tumbling count using ANN was carried out by Kanchan and Maniyeri [24]. Recently, Ntetsika and Papadopoulos [25] predicted filament orbit classes using ANN. The oscillation frequency of elastic plate subjected to viscous flow and corresponding fluid-induced deformation was studied by Kanchan et al. [26, 27]. When analyzing the above literature, it is quite clear that most of the studies have relied upon ANN for predicting the results, especially in the case of parametric immersed boundary simulation studies.

It is evident that flexible filaments when subjected to shear flow deform to produce various orbit classes which are dependent on magnitude of shear flow, elastic and bending rigidity of the flexible structure, the length of the filament and initial position with respect to flow. Very few studies have investigated the tumbling, buckling, recuperation and mutual interaction dynamics of two filaments placed side-by-side in shear flow. The observations from such studies will help in designing microfluidic devices for cell/particle sorting where multiple flexible filaments can be utilized and particles of various sizes can be sorted. In order to address this issue, we perform detailed parametric simulations using formally second-order accurate IBM proposed in our previous study [28]. From the perspective of utilizing machine learning algorithms to assist in simulation tasks, it is evident that ANN's produce reliable results due to its improved accuracy, flexibility and faster workflows. However, it is also important to note that ANN's are prone to overfitting, highly sensitive to hyperparameters and require large amount of high-quality data to produce reasonably accurate results. There is a need to understand how other machine learning algorithms perform with the available simulation data. To ensure a comprehensive and robust evaluation, five classification algorithms were selected—Naive Bayes, Support Vector Machine (SVM), Decision Tree, k-Nearest Neighbors (KNN), and Artificial Neural Network (ANN)—based on their distinct modelling paradigms. Naive Bayes, a probabilistic classifier that assumes feature independence, is valued for its simplicity, interpretability, and computational efficiency. SVM is capable of handling both linear and nonlinear classification tasks through kernel functions and is particularly effective in high-dimensional spaces. Decision Tree constructs hierarchical, rule-based models that capture nonlinear patterns via recursive data partitioning. KNN, a non-parametric and instance-based approach, classifies samples based on proximity in the feature space, leveraging local structure. ANN, implemented as a multilayer perceptron, models complex nonlinear relationships and has been previously applied in fluid–structure interaction (FSI) contexts, although it typically requires careful parameter tuning and sufficient data. The use of these diverse classifiers enables a balanced assessment of predictive accuracy, interpretability, and generalization ability across algorithmic types when applied to features derived from FSI simulations. In this work, filament orbit classes of first and second filaments are obtained from IBM simulation and used to train- test machining learning (ML) models mentioned above; then systematically compared with the results obtained from ANN. These mentioned aspects serve as the prime motivation for the present study. From the literature review it is found that comparison of ML models with ANN model for the case of flexible filaments deformation in shear flow using IBM simulation data is not reported so far which is the novelty of the present work.

2. Methodology

2.1. IBM numerical procedure

The fluid domain is made of Cartesian co-ordinates $\boldsymbol{x}^* = (x^*, y^*)$ while the flexible filament is modelled using one-dimensional Lagrangian markers denoted by $X^* = (s^*, t^*)$. The material points at given time instance t^* are represented by parameter s^*. The two-way coupled interaction between the flexible filament and surrounding viscous fluid flow is implemented using the formally second-order IBM used in our previous study [28]. The physical parameters used in the simulation of two side-by-side filaments are depicted in Table 1. The dimensional quantities are denoted with $*$ symbol. The values of parameters chosen in the present study are taken from experimental studies involving synthetic fibers such as rayon or dacron, immersed in highly viscous fluids such as corn syrup or castor oil. These values were used earlier [18] to simulate pulp fibers immersed in viscous fluids. Therefore, considering the realistic physical attributes of the system, the said parameters are chosen for our study.

A linear shear flow velocity profile is provided at the channel inlet given by Eq. (2):

$$u^* = \left(y^* - \frac{H_c^*}{2}\right) \times G^* \tag{2}$$

where, $G^* = \frac{2u^* u_{wall}^*}{H_c^*}$.

Table 1. The physical parameters.

Physical parameters	Dimensional values
Channel height (H_c^*)	0.5 cm
Channel width (L_c^*)	2.0 cm
Fluid density (ρ)	1.0 $\frac{g}{cm^3}$
Fluid viscosity (μ)	8 – 10 $\frac{g}{cm.s}$
Shear rate (G^*)	8 – 64 $\frac{1}{s}$
Filament length (L^*)	0.1 – 0.3 cm
Bending stiffness (K_b^*)	1.0 – 5.0 × 10^{-4} $\frac{g}{cm^2 s^2}$
Distance between filament mid-points (D^*)	0.3 cm

With respect to reference scales U_{ref}, L_{ref}, the non-dimensional continuity and Navier-Stokes equation are provided in Eqs. (3) and (4), respectively:

$$\nabla . u = 0 \tag{3}$$

$$\frac{\partial u}{\partial t} + u.\nabla u = -\nabla p + \frac{1}{\mathrm{Re}}\nabla^2 u + f \tag{4}$$

where, Re is the Reynolds number given by Eq. (5):

$$\mathrm{Re} = \frac{\rho U_{ref} L_{ref}}{\mu} \tag{5}$$

and f denotes Eulerian force density. The Eulerian force density f is added to Eq. (4) to describe the structural forces exerted by the flexible filament on the fluid region. This term is provided in Eq. (6):

$$f(x,t) = \int \boldsymbol{F}(s,t)\delta(x - X(s,t))\ ds \tag{6}$$

where, $\boldsymbol{F}(s,t)$ is defined as the Lagrangian force term which is used to define the mechanical properties of the filament such as stretching, bending etc. The filament is made up of a series of Lagrangian points connected by linkages have resting length Δs. The expression for Lagrangian force term is given in Eq. (7):

$$\boldsymbol{F}(s,t) = -\frac{\partial E(X(s,t))}{\partial X} \tag{7}$$

In Eq. (7), the elastic energy functional E is defined in its variational derivative form. The elastic energy functional in this study is made up of resistance forces related to stretching/compression and bending and provided in Eq. (8):

$$E(X(s,t)) = \frac{1}{2}\int K_s\left(\left|\frac{\partial X}{\partial s}\right| - 1\right) ds + \frac{1}{2}\int K_b\left(\frac{|\partial^2 X|}{\partial s^2}\right) ds \tag{8}$$

where, K_s and K_b are the stretching and bending coefficients, respectively. The stretching coefficient K_s is assumed to be large value that satisfied the inextensibility condition of the filament. Therefore, it is possible to calculate the Lagrangian force term $\boldsymbol{F}$ by solving Eq. (7). This in turn provides necessary input to Eq. (6) and the solution of Eq. (6) is added as the Eulerian force density f in Navier-Stokes equations.

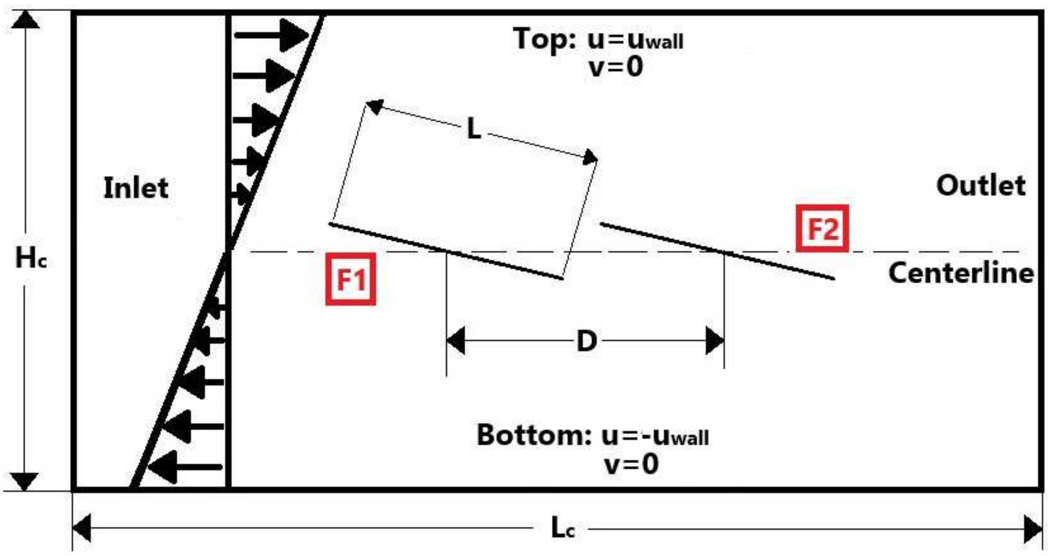

Fig. 1. Schematic representation of two side-by-side untethered flexible filaments subjected to viscous shear flow and parameters defined in Table 1.

Once the new fluid variable $\boldsymbol{u}(x,t)$ is obtained at next time step, which is the solution of Eq. (4), the velocity of flexible filament $\boldsymbol{U}(s,t)$ can be obtained from Eq. (9). Once the velocity of flexible filament is known, the modified position of the filament can be determined:

$$\boldsymbol{U}(x,t) = \int u(s,t)\delta(x - X(s,t))dx \tag{9}$$

where, $\delta(x)$ is the dirac-delta distribution function given by Eq. (10):

$$\delta(x) = \frac{1}{h^2}\varphi\left(\frac{x}{h}\right)\varphi\left(\frac{y}{h}\right) \tag{10}$$

where, h is the fluid mesh width and $\varphi(r)$ is a function given by Eq. (11):

$$\varphi(r) = \begin{cases} \frac{1}{4}\left(1+\cos\left(\frac{\pi r}{2}\right)\right), & \text{if } |r| \le 2 \\ 0, & \text{if } |r| > 2 \end{cases} \tag{11}$$

Thus, a two-way coupling between fluid and structure is achieved. In order to improve accuracy, the numerical scheme employed in the present study is formally second order in nature. The time advancement is achieved by dividing it into two stages. In the first stage, with reference to information available at time level 'n', the time step is advanced to '$n+\frac{1}{2}$' level. The governing equations given in Eq. (3) and Eq. (4) are discretized and solved to new timestep as shown in Eq. (12) and Eq. (13). The motion of the flexible filament is calculated using the discretized equation given in Eq. (14) and Eq. (15). The Eulerian and Lagrangian force density terms are updated as shown in Eq. (16) and Eq. (17), respectively:

$$(\nabla u)^{n+\frac{1}{2}} = 0 \tag{12}$$

$$\frac{u^{n+\frac{1}{2}} - u^n}{\left(\frac{\Delta t}{2}\right)} + (u.\nabla u)^n = -\nabla p^n + \frac{1}{\mathrm{Re}}\nabla^2 u^n + f^n \tag{13}$$

$$U^{n+\frac{1}{2}} = \sum_h u^{n+\frac{1}{2}}\delta(x - X^n)h^2 \tag{14}$$

$$\frac{X^{n+\frac{1}{2}} - X^n}{\left(\frac{\Delta t}{2}\right)} = U^{n+\frac{1}{2}} \tag{15}$$

$$F^{n+\frac{1}{2}} = -\frac{\partial E(X^{n+\frac{1}{2}})}{\partial X} \tag{16}$$

$$f^{n+\frac{1}{2}} = \sum_S F^{n+\frac{1}{2}}\delta(x - X^n)ds \tag{17}$$

With the completion of first step, the solutions obtained from Eq. (12) to Eq. (17) are updated to new time step $(n+1)$ in the second time-step stage. The details of this updation are provided from Eq. (18) to Eq. (23):

$$(\nabla.u)^{n+1} = 0 \tag{18}$$

$$\frac{u^{n+1} - u^n}{(\Delta t)} + (u.\nabla u)^{n+\frac{1}{2}} = -\nabla p^{n+\frac{1}{2}} + \frac{1}{\mathrm{Re}}\nabla^2 u^{n+\frac{1}{2}} + f^{n+\frac{1}{2}} \tag{19}$$

$$U^{n+1} = \sum_h u^{n+1}\delta\left(x - X^{n+\frac{1}{2}}\right)h^2 \tag{20}$$

$$\frac{X^{n+1} - X^n}{(\Delta t)} = U^{n+1} \tag{21}$$

$$F^{n+1} = -\frac{\partial E(X^{n+1})}{\partial X} \tag{22}$$

$$f^{n+1} = \sum_S F^{n+1}\delta(x - X^{n+1})ds \tag{23}$$

This denotes the end of second stage and the numerical scheme proceeds until convergence condition is achieved. The spatial discretization is done as per finite volume scheme and temporal discretization is implicit in nature. The deferred correction second-order differencing scheme of Hayase et al. [29] is used to treat the convection and diffusion fluxes. The governing momentum equation are solved using SIMPLE algorithm. The continuity is maintained by solving pseudo-pressure Poisson Equation using ICCG algorithm. The initial condition for solving pseudo-pressure is based on the intermediate velocity obtained from initially guessed pressure values. The obtained pressure from Poisson equation and guessed pressure are added together to obtain actual pressure. The actual pressure obtained is used to calculate velocity components in x and y directions, and the solution is maintained divergence free. The inlet and outlet channel walls are subjected to periodic boundary conditions whereas the inlet and outlet walls of the channel are provided with no-slip boundary condition. A two-stage algorithm that describes the implementation of formally second-order immersed boundary method is given below:

Stage 1:

Input data to Stage 1 includes variables such as fluid velocity $\boldsymbol{u}^{\boldsymbol{n}}$, pressure p^n, filament deformation $\boldsymbol{X}^{\boldsymbol{n}}$ and Eulerian force density $\boldsymbol{f}^{\boldsymbol{n}}$.

Step 1: The intermediate fluid velocity $\boldsymbol{u}^{n+\frac{1}{2}}$, is calculated using Eq. (12) and Eq. (13).

Step 2: The computed velocity in Step 1 is interpolated to Lagrangian grid to obtain filament velocity $\boldsymbol{U}^{n+\frac{1}{2}}$ and filament position $\boldsymbol{X}^{n+\frac{1}{2}}$ using Eq. (14) and Eq. (15).

Step 3: Subsequently, the elastic forces of filament $\boldsymbol{F}^{n+\frac{1}{2}}$ are computed in Eq. (16) and distributed onto the Eulerian fluid grid using Eq. (17) by calculating the force density term $\boldsymbol{f}^{n+\frac{1}{2}}$. This marks the end of Stage 1.

Stage 2:

Input data to Stage 2 includes output of Stage 1 variables such as fluid velocity $\boldsymbol{u}^{n+\frac{1}{2}}$, pressure $p^{n+\frac{1}{2}}$, filament deformation $\boldsymbol{X}^{n+\frac{1}{2}}$ and Eulerian force density $\boldsymbol{f}^{n+\frac{1}{2}}$.

Step 4: The final fluid velocity $\boldsymbol{u}^{n+1}$, is calculated using Eq. (18) and Eq. (19).

Step 5: The computed velocity in Step 4 is interpolated to Lagrangian grid to obtain final filament velocity $\boldsymbol{U}^{n+1}$ and filament position $\boldsymbol{X}^{n+1}$ using Eq. (20) and Eq. (21).

Step 6: Finally, the elastic forces of filament $\boldsymbol{F}^{n+1}$are computed in Eq. (22) and distributed onto the Eulerian fluid grid using Eq. (23) by calculating the force density term $\boldsymbol{f}^{n+1}$. This marks the end of Stage 2.

The convergence criteria are checked and if not achieved the process is repeated until convergence is met. Based on the physical parameters specified in Table 1, two-dimensional numerical simulation of two side-by-side flexible filaments placed without any constraints and subjected to viscous shear flow is carried out. The simulation is performed on a computational domain as shown in Fig. 1. Both the filaments are initially inclined by about 5° with respect to horizontal so as to initiate the deformation process by inducing asymmetry in the filament motion. The computational model used in the present study has been extensively validated for a variety of FSI problems, details of which can be found in our previous studies [20, 26, 28]. Based on the inextensibility test and grid refinement procedures carried out in previous studies [24], a uniform computational grid of 512 × 128 is chosen here. Both the flexible filaments are made up of 100 immersed boundary points thus containing 99 linkages between them. The domain size, range of filament length, fluid shear rate, bending rigidity and distance of separation between the two filaments for carrying out parametric studies are specified in Table 1 and suitably non-dimensionalzed with respect to reference parameters. For all simulations, the CFL number is maintained less than 1 and simulations for all cases are performed for fixed time t = 3.0 with time step $t = 1\times10^{-5}$.

3. Results and Discussions

3.1. Two side-by-side flexible filament orbits

In the present study, parametric analysis is carried out by considering three filament lengths (L = 0.1, 0.2, 0.3), three shear rates (G = 8, 16, 32) and 16 different values of filament bending rigidity K_b. From the numerical studies of Stokie and Green [18], followed by our recent study [20], the deformation of flexible filaments is categorized into orbit classes by calculating the exterior angle (β). These deformations of flexible filament can be grouped into classes i.e. Rigid, Springy, C-shape, S-shape and Complex. When two flexible filaments are placed side-by-side in shear flow, similar orbit classes are obtained for both filaments. Figure 2 shows the various deformation observed for both the filaments. The deformation in first row is attributed to filament 1 (F1) and second row is filament 2 (F2) respectively. In Fig. 2(a), the rigid motion of filaments is shown. The filaments are initially placed at an inclination angle with respect to horizontal, complete clockwise rotation at t = 0.9. The filament appears to be straight with negligible bending. The springy motion of filaments is observed in Fig. 2(b) where the filaments centre portion undergoes buckling at t = 0.55. The filament recovers from this position and retains original shape at time t = 0.75. The rotation completes faster as compared to rigid case. An interesting feature is observed in Fig. 2(c) where the first filament undergoes C-shape deformation, and second filament produces S-shape motion at time t = 0.5. Various forms of filament deformations are observed starting from t = 0.3 to t = 0.7. However, the filaments recover back to their original state and an elastic type of deformation is seen. Finally, in Fig. 2(d) the deformation of flexible filament into complex shapes is observed. The filaments are completely deformed and never return to their original shape. The structural elastic forces (F_E) in rigid and springy cases resist hydrodynamics forces (F_H) and thus return to their original shape whereas in complex deformation the structural forces are too weak to offer any resistance. The demarcation of filaments dynamic behaviour can be approximated to a flow-filament offset ratio given by Eq. (24):

$$\varphi = \frac{F_H}{F_E} = \frac{\mu G^*}{\left(\frac{K_b^*}{(L^*)^3}\right)} \tag{24}$$

When observing Fig. 2(e), it can be noted that at time t = 0.25, two recirculation zones are formed, one near the leading side and other close to the trailing side. As time progresses, the recirculation zone near the leading side increases in size while the one close to the trailing side diminishes. The filament breaks symmetry at time t = 0.46, and is unable to resist the hydrodynamic forces and aligns itself along the zone edges. At time t = 0.5, the recirculation zone has gained the maximum size depicting an eye shape and filament coils around the zone center. The filament finally untangles itself at time t = 0.65 with respect to reducing zone size and reaches equilibrium straight line configuration at time t = 0.85. As shown in Fig. 2(f), the leading and trailing ends of flexible filament are subjected to recirculation zones at time t = 0.22. The trailing end zone is larger in size which initiates the coiling of filament. The coiling continues with time and at t = 0.44, the leading side zone completely diminishes. At t = 0.56, the large recirculation zone splits temporarily into two attached small zones and the filament aligns along the zone edges, with the leading end undergoing significant bending thus depicting S-shape. Next, the zones merge back together and recirculation zone moves towards the leading end of filament simultaneously uncoiling the filament. Finally, at time t > 0.7, the filament untangles completely and reaches equilibrium position.

From Eq. (24), it is quite evident that as the filament transition occurs from rigid to complex deformation, the structural forces decrease and there is reduction in resistance to hydrodynamic forces. The demarcation of first filament F1 and second filament F2 orbit classes for varying shear rate and filament lengths can be visualized using colormaps shown in Fig. 3 and Fig. 4, respectively. The colormaps of F1 and F2 can be divided into 9 sub-groups. The sub-groups can be named horizontally starting with bottom left all the way to top right.

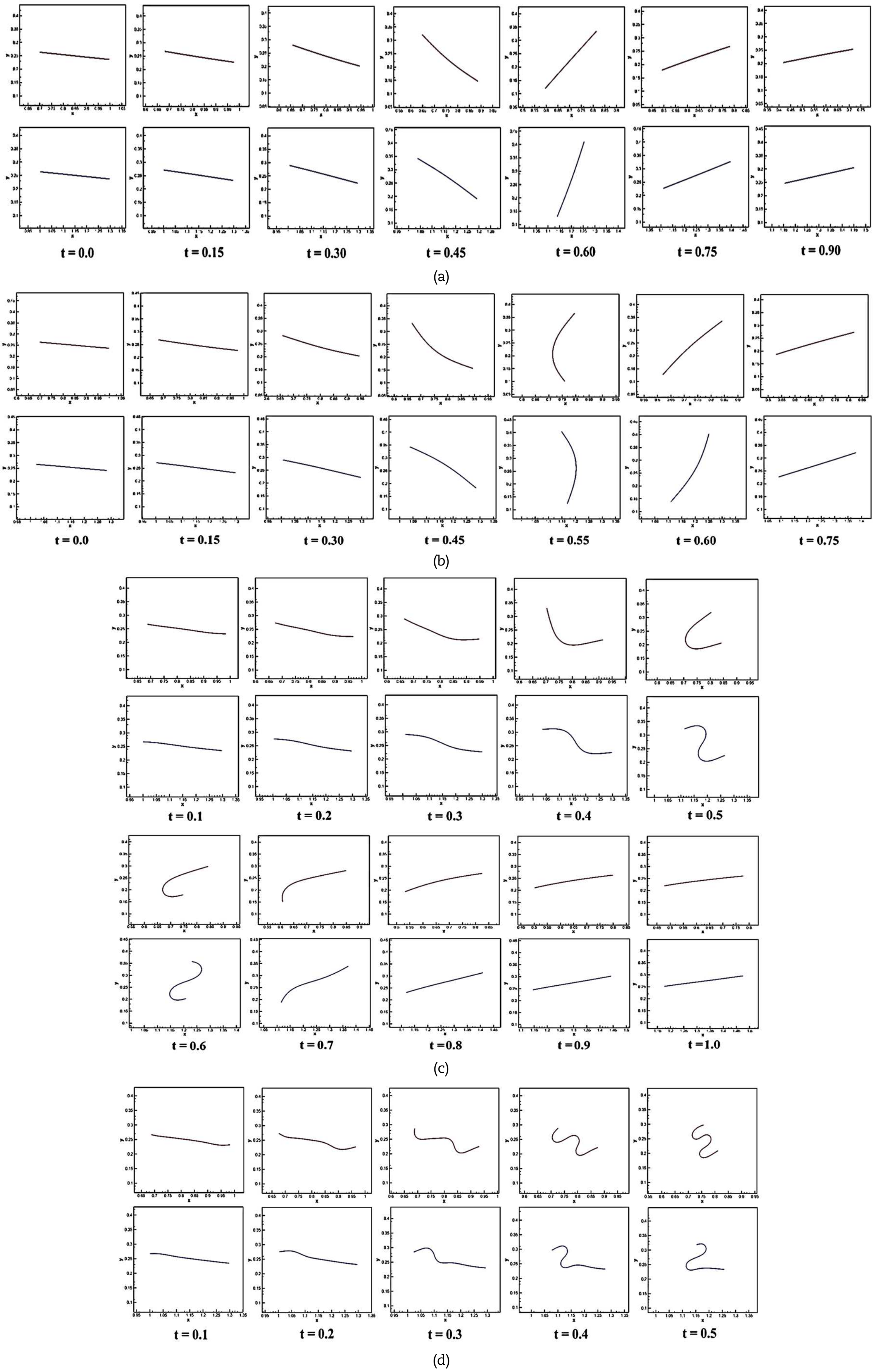

Fig. 2. (a-d) Flexible filament deformations of F1 in first row and F2 in second row grouped into various orbit classes at different time instances, (a) Rigid deformation (L = 0.3, G = 8, K_b = 0.5), (b) Springy deformation (L = 0.3, G = 16, K_b = 0.5), (c) First filament undergoing C-shape deformation and second filament S-shape (L = 0.3, G = 16, K_b = 0.5), (d) Complex deformation (L = 0.3, G = 16, K_b = 0.01), (e-f) Streamlines obtained close to the filament during the formation of C-shape and S-shape at different time intervals, (e) C-shape formation, (f) S-shape formation.

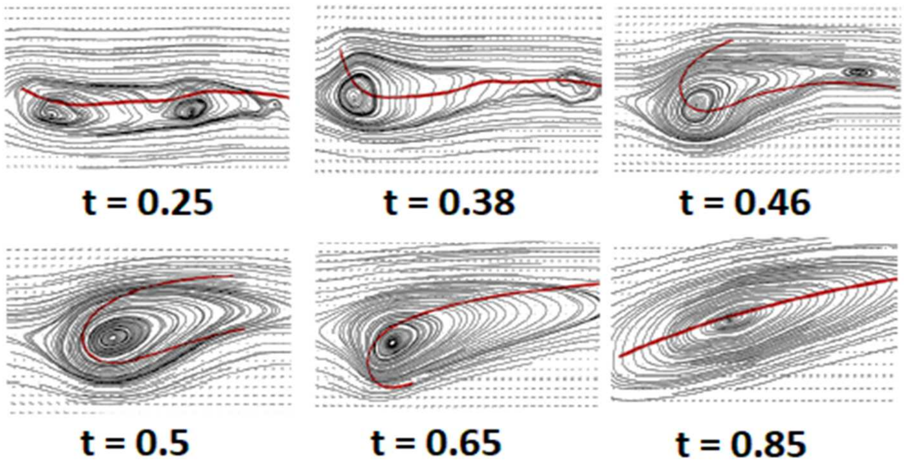

(e)

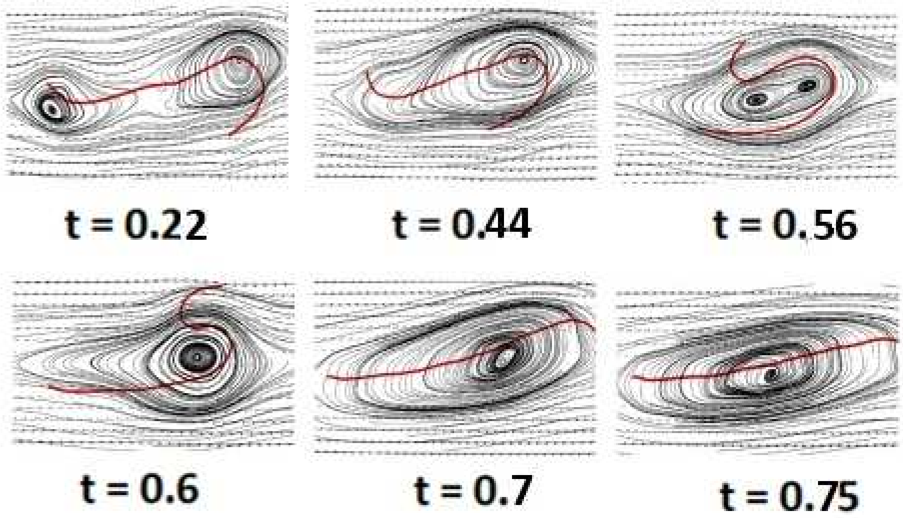

(f)

Fig. 2. Continued.

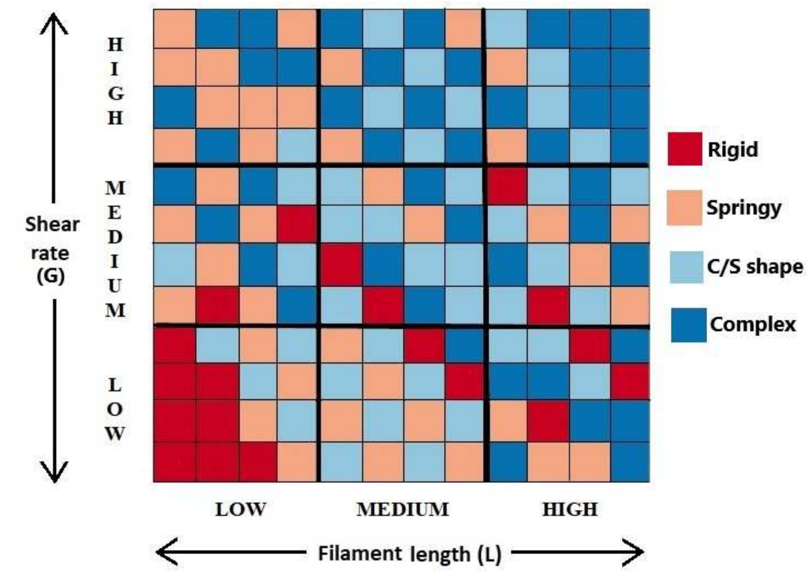

Fig. 3. The colormap showing filament orbit classes of F1 for varying shear rate and filament length values.

Accordingly, the sub-group can be designated LL, LM and LH indicating the bottom sub-groups having low shear rate and low, medium and high filament lengths, respectively. The designation for middle sub-groups will be ML, MM and MH indicating medium shear and low, medium and high filament lengths. Lastly, the top sub-groups can be named as HL, HM and HH, respectively.

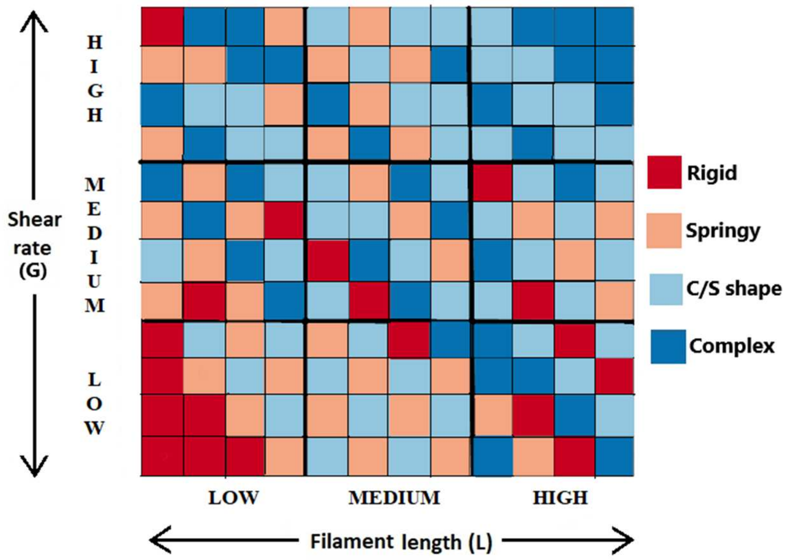

Fig. 4. The colormap showing filament orbit classes of F2 for varying shear rate and filament length values.

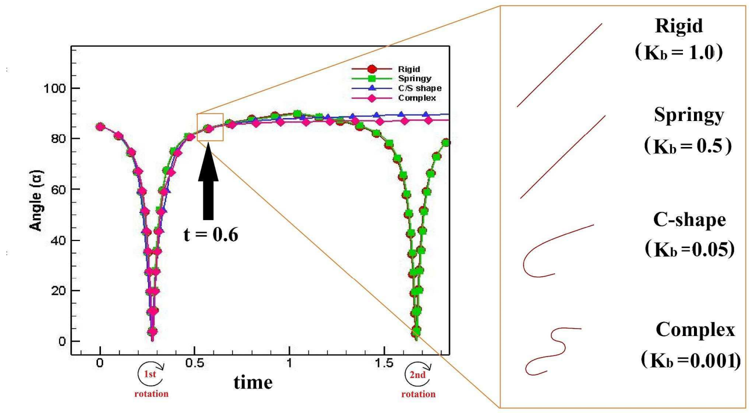

Fig. 5. First filament (F1) deformations at time t = 0.6 with conditions L = 0.3 and G = 16.

From the figures, it is clear that LL sub-group is dominated by rigid deformations whereas HH leads to complex shape deformations in both F1 and F2. In the first filament, springy deformation is found to be widely spread in ML and HL sub-groups and in the transition regions between LL and LM sub-groups. When comparing F1 with F2, in ML and HL sub-groups, the springy deformations are replaced by C-shape/S-shape and Complex deformations. This indicates that at high shear rates, the first filament deformation has negligible effect on the deformation of second filament. However, in the transition regions between LL and LM sub-groups, the distribution of springy behaviour in F2 is similar to that of F1. In HM sub-group of F1, C-shape/S-shape and Complex deformation is found to be dominant while in HM sub-group of F2, some of the C-shape/S-shape orbits are replaced by springy motion. This is clear evidence that for the same set of parameters the first filament reduces the hydrodynamic force acting on the second filament and thus springy nature is observed in second filament. Rigid deformations in the diagonal regions close to MM sub-groups are found in both F1 and F2. Another aspect to be observed while comparing HH sub-group of both F1 and F2 is that Springy deformations are replaced by C-shape/S-shape deformations. These results indicate that at higher shear rates and high filament lengths, there is much less effect of first filament on the surrounding hydrodynamic forces and the deformation of second filament is not influenced by first filament. From the above discussion it is quite evident that for the first filament to exert any influence on the second filament deformation, the filament length should be medium ($L \approx 0.2$) and high shear rate ($G \approx 32$).

The deformation of F1 and F2 for fixed length L = 0.2 and fixed shear G = 16 is shown in Fig. 5 and Fig. 6, respectively. The first and second rotation of F1 is shown in Fig. 5 and time interval between successive rotations is found to be 1.4 for this case. At time t = 0.6, the first filament shows C-shape orbit while second filament shows S-shape deformation. Another observation is that there are multiple buckle points at K_b = 0.001 for F1 as compared to F2. Also, second filament produces only one rotation during the entire period of observation indicating that multiple buckle points induce faster tumbling or rotation as compared to simple buckle shapes in complex orbits.

Based on the studies of Stockie and Green [18], the probability distribution of time taken by F1 filament at different tumbling angles (α) for varying shear rate (G) is shown in Fig. 7 and Fig. 8 for rigid deformation and complex deformation, respectively. Since, α is defined with respect to the vertical, tumbling angle of 0° indicates the filament is vertically placed perpendicular to fluid flow and 90° tumble angle signifies that the filament is placed horizontal, parallel to fluid flow. It can be seen in Fig. 7 that rigid filament at high shear tend to remain horizontal for longer period than at low shear. This means that rigid filaments at low shear undergoes more tumbling count per unit time. The difference in time duration for which F1 remains horizontal between G = 8 and G = 32 is quite substantial. However, in Fig. 8 the time difference between low and high shear rates are small for complex deforming filaments. Contrary to rigid filaments, complex deformation filaments at low shear tend to remain in the horizontal position longer than at high shear. Due to highly buckled state of complex deformed filaments, tumbling count increases with increase in shear rate.

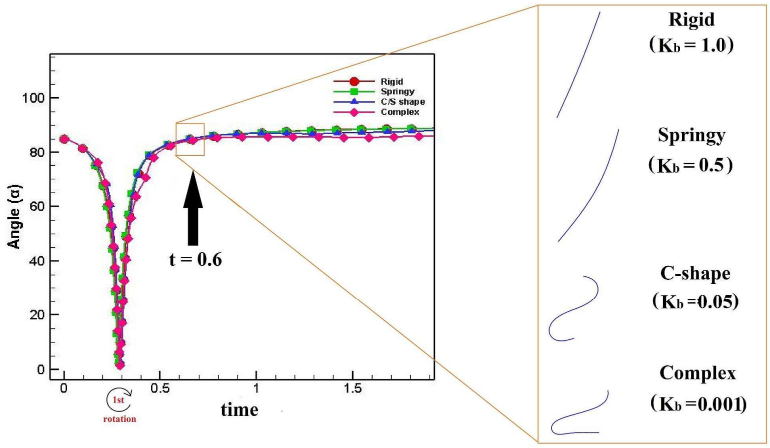

Fig. 6. Second filament (F2) deformations at time t = 0.6 with conditions L = 0.3 and G = 16.

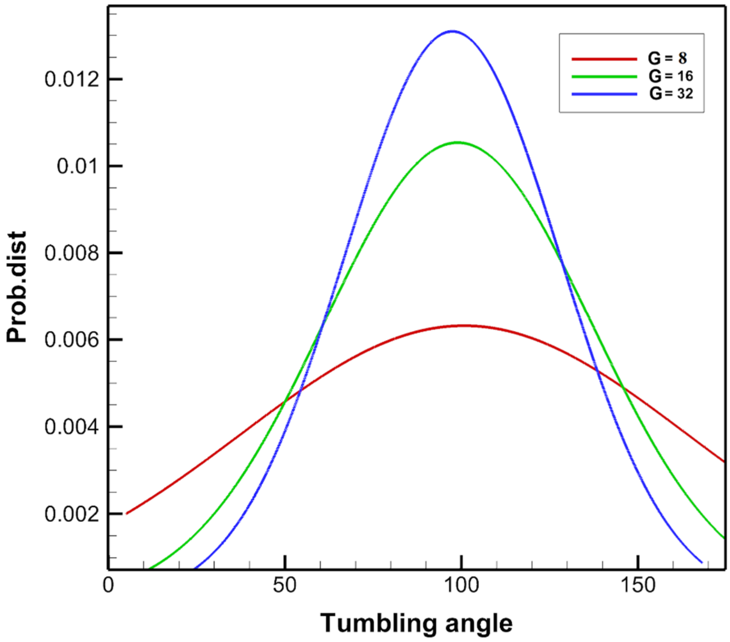

Fig. 7. Probability distribution of time taken by a rigidly deforming filament at various shear rates (G).

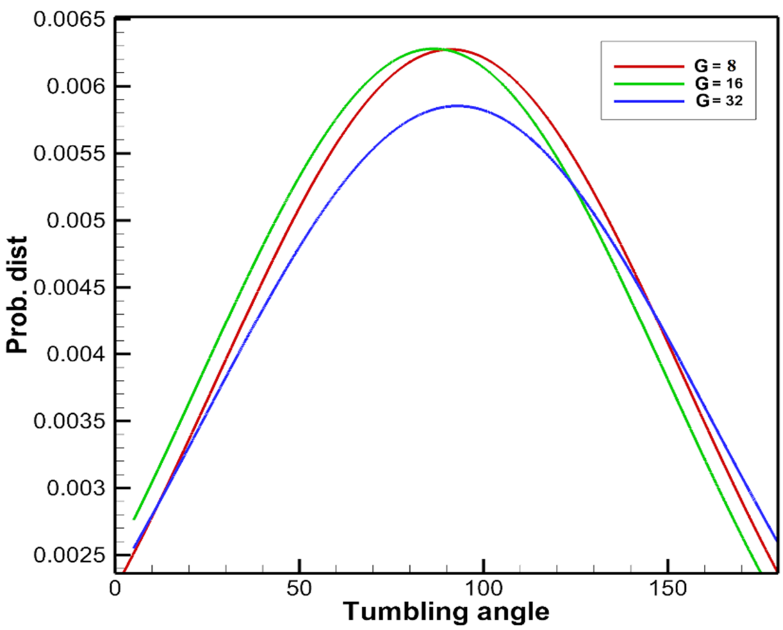

Fig. 8. Probability distribution of time taken by a complex deforming filament at various shear rates (G).

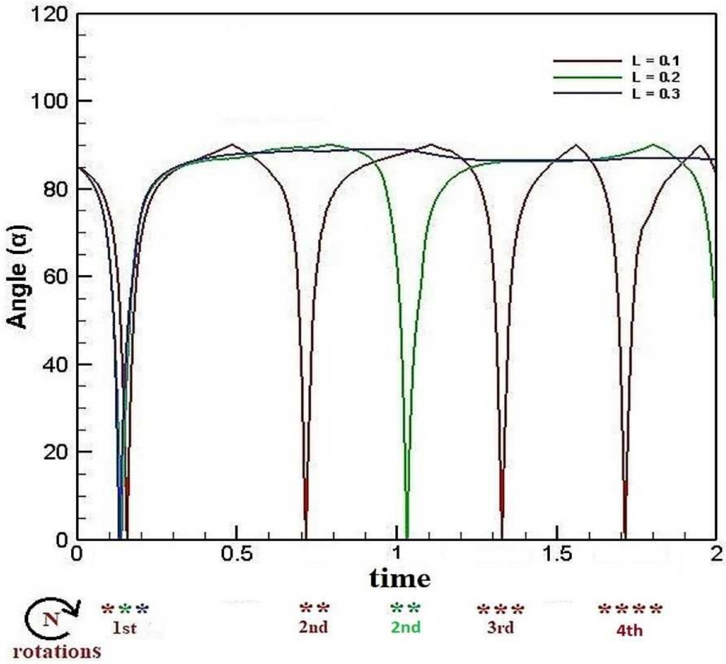

Fig. 9. Inclination angle with respect to time for fixed shear G = 32, K_b = 0.05 and varying lengths of first filament (F1). The number of tumbling rotations observed along the time span is marked on x-axis.

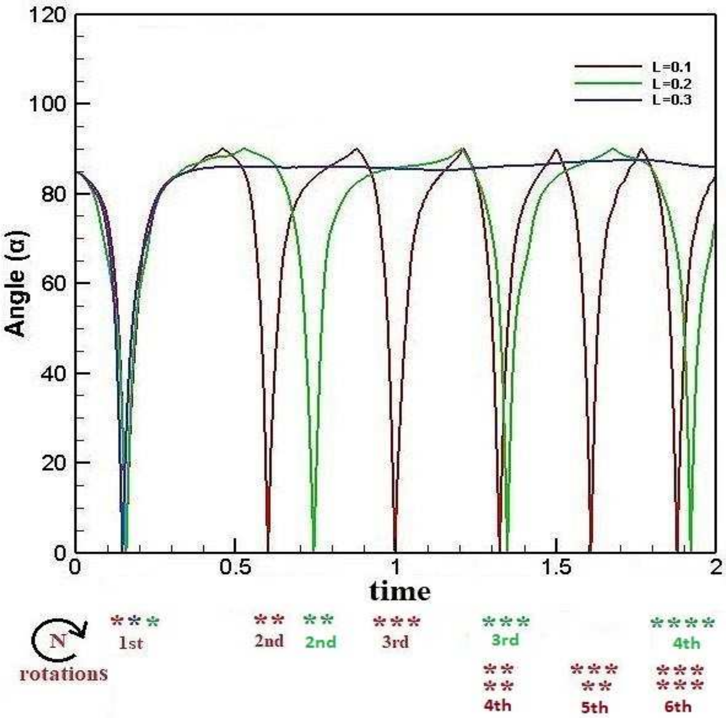

Fig. 10. Inclination angle with respect to time for fixed shear G = 32, K_b = 0.05 and varying lengths of second filament (F2). The number of tumbling rotations observed along the time span is marked on x-axis.

The effect of filament length (L) on the inclination angle for G = 32 and K_b = 0.05 is captured in Fig. 9 and Fig. 10 for F1 and F2, respectively. In Fig. 9, for the total observational duration of time t = 2.0, shorter filament L = 0.1 undergoes four rotations, while L = 0.2 undergoes two rotations and L = 0.3 only one rotation. Since the shear rate is high, shorter filaments are not able to resist hydrodynamic forces and tend to undergo substantial tumbling. On the other hand, F2 undergoes six rotations for L = 0.1, four rotations for L = 0.2 and one rotation for L = 0.3. This clearly reconfirms from previous discussions that at high shear rate, the influence of first filament on the deformation of second is marginal. For the same conditions, the number of tumbling rotations increases in second filament for L = 0.1 and L = 0.2 as compared to that of first filament.

The effect of shear rate (G) on the inclination angle for L = 0.1 and K_b = 0.025 is captured in Fig. 11 and Fig. 12 for F1 and F2, respectively. In Fig. 11, the filament at higher shear rate (G = 32) tumbles faster, followed by G = 16 and lastly by G = 8. There is no overlap of tumbling or rotation as seen in Fig. 9. The filament at high shear undergoes four rotations, whereas intermediate shear and low shear filaments achieve two rotations and one rotation respectively, over the entire observational time. In Fig. 12, the time taken by high and intermediate shear filament to tumble is similar to that of first filament.

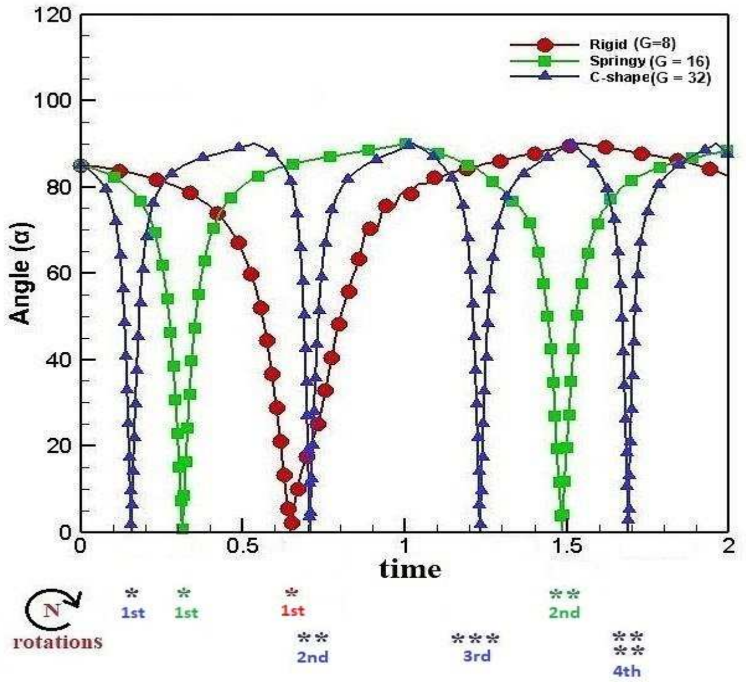

Fig. 11. Inclination angle with respect to time for fixed length $L = 0.1$, $K_b = 0.025$ and varying shear rates of first filament (F1). The number of tumbling rotations observed along the time span is marked on x-axis.

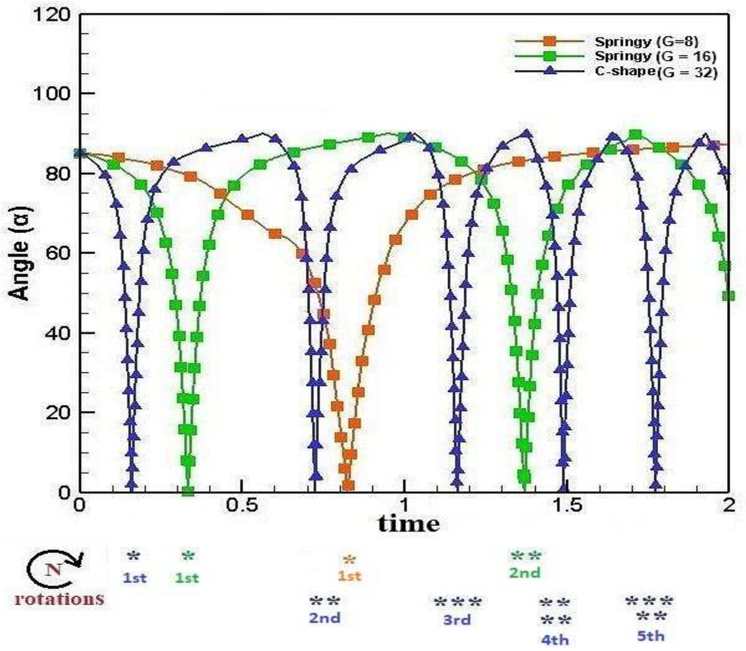

Fig. 12. Inclination angle with respect to time for fixed shear $L = 0.1$, $K_b = 0.025$ and varying shear rates of second filament (F2). The number of tumbling rotations observed along the time span is marked on x-axis.

Even the shape formations are the same at $G = 16$ and $G = 32$ for both filaments. However, the second filament never produces rigid orbit at low shear. The filament at high shear undergoes five rotations, whereas intermediate shear and low shear filaments achieve two rotations and one rotation respectively, over the entire observational time. This clearly indicates that the first filament is subjected to higher hydrodynamic forces as compared to second filament. Also, the presence of the first filament delays tumbling of the second filament as seen in Fig. 12 for case $G = 8$.

The Fast Fourier Transform (FFT) plot and spectrogram plot for deformations of F1 and F2 at fixed length ($L = 0.3$) and varying shear rates are shown in Fig. 13 and Fig. 14, respectively. In Fig. 13, no significant peaks in frequency are observed. In spectrogram plot it is observed that, at $G = 8$, there are two energy bands at large distances while the number of energy bands increases with increase in shear rate. There are six bands at $G = 16$ and 14 bands at $G = 32$. For all the cases it can be seen that the distance between first and second band is large and the distance between successive bands either remains same or decreases. It becomes clear that after 3 or 4 energy bands, and at especially high shear, recurring displacement of filament occur without retardation. Therefore, any attempt to restrict motion has to be achieved before the deformation reaches 3rd band. In Fig. 14, when energy bands are seen for F2, the distance between energy gap shortens rapidly after 2nd band itself ($G = 32$). However, there is sufficient band gap between energies at low and intermediate shear.

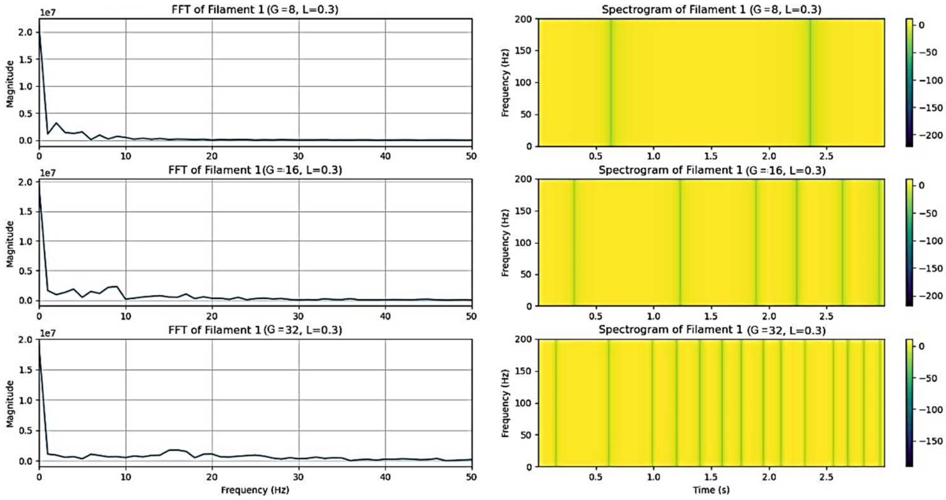

Fig. 13. FFT of filament deformation and spectrogram plot for first filament at fixed length (L = 0.3) and varying shear rate.

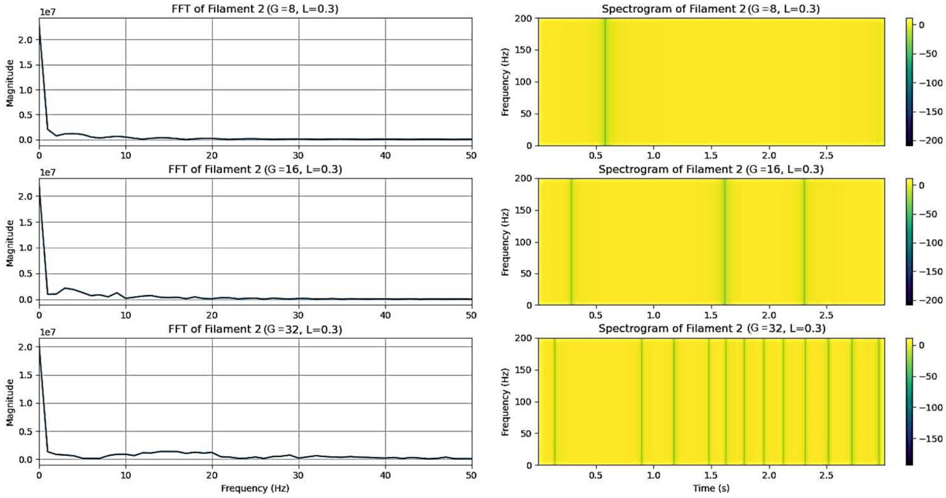

Fig. 14. FFT of filament deformation and spectrogram plot for second filament at fixed length (L = 0.3) and varying shear rate.

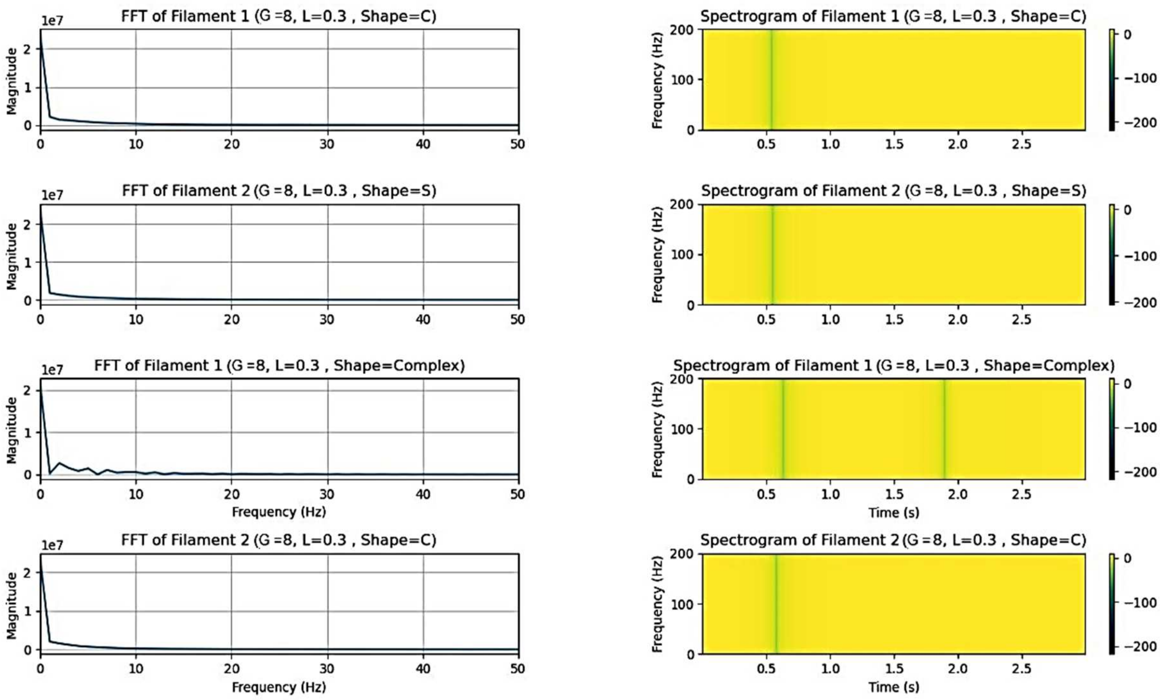

Fig. 15. FFT of filament deformation and spectrogram plot for F1 and F2 in order of shape formation for G = 8 and L = 0.3.

The deformation FFT plot and spectrogram plot for F1 and F2 at G = 8 and L = 0.3 for various shapes are shown in Fig. 15. In all cases for C-shape deformation the frequency plot is smooth indicating a single dominant frequency. Also, there is a single energy band. For complex orbit, however, quasi-static multiple frequencies are observed and the number of energy bands are two indicating higher energy release. The same observation is seen for G = 16 in Fig. 16 and G = 32 in Fig. 17 when C-shape deformation is compared with that of Complex shape. As seen in Fig. 16, for Complex deformation, a high energy band is obtained near the end of simulation indicating the onset of high frequency deformations. In Fig. 17, high energy region is obtained for F2 undergoing C-shape orbit. Another observation in Fig. 17 at high shear (G = 32), F1 undergoing Complex deformation produces large number of energy bands whereas the F2 produces only 2 wide spaced bands with C-Shape. This is evidence that F1 has a predominant role to play in the deformation of F2 at high shear. F1 absorbs hydrodynamic forces resulting in multiple energy band formations whereas the second filament (F2) receives lower levels of fluid forces, thus leading to C-shape formations and that too with large band gaps. These observations will help in designing microfluidic devices for cell/particle sorting where multiple flexible filaments can be utilized and particles of various sizes can be sorted.

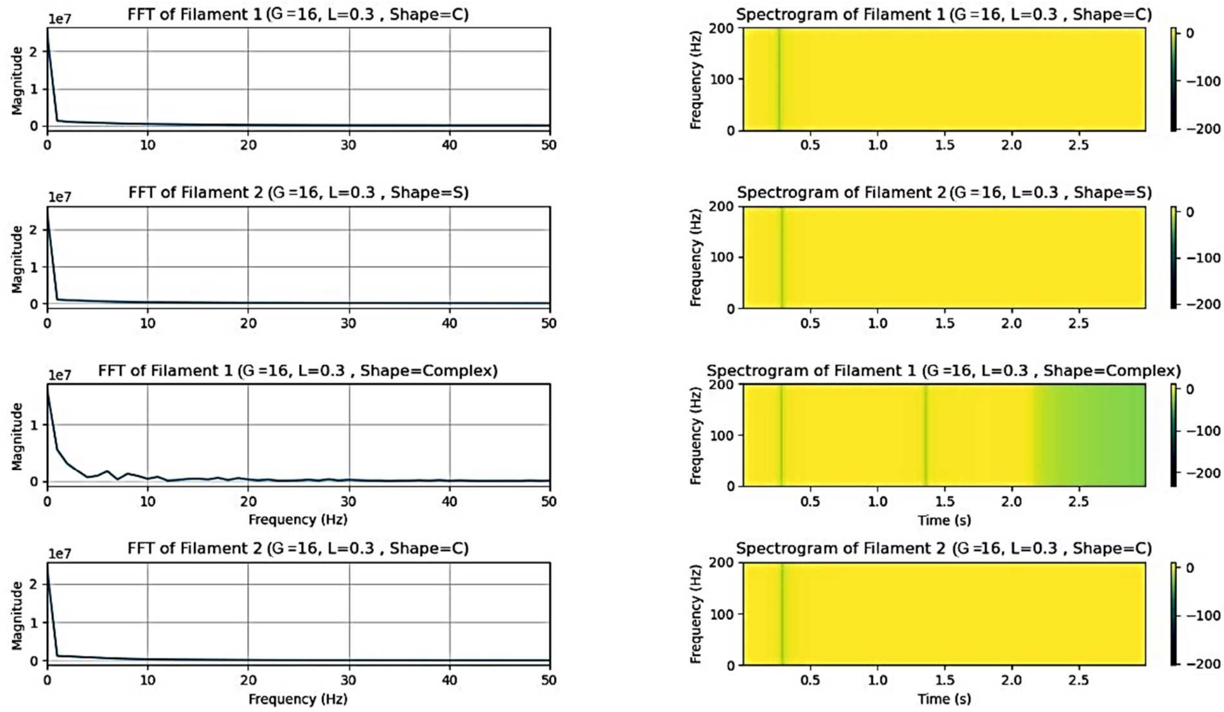

Fig. 16. FFT of filament deformation and spectrogram plot for F1 and F2 in order of shape formation for G = 16 and L = 0.3.

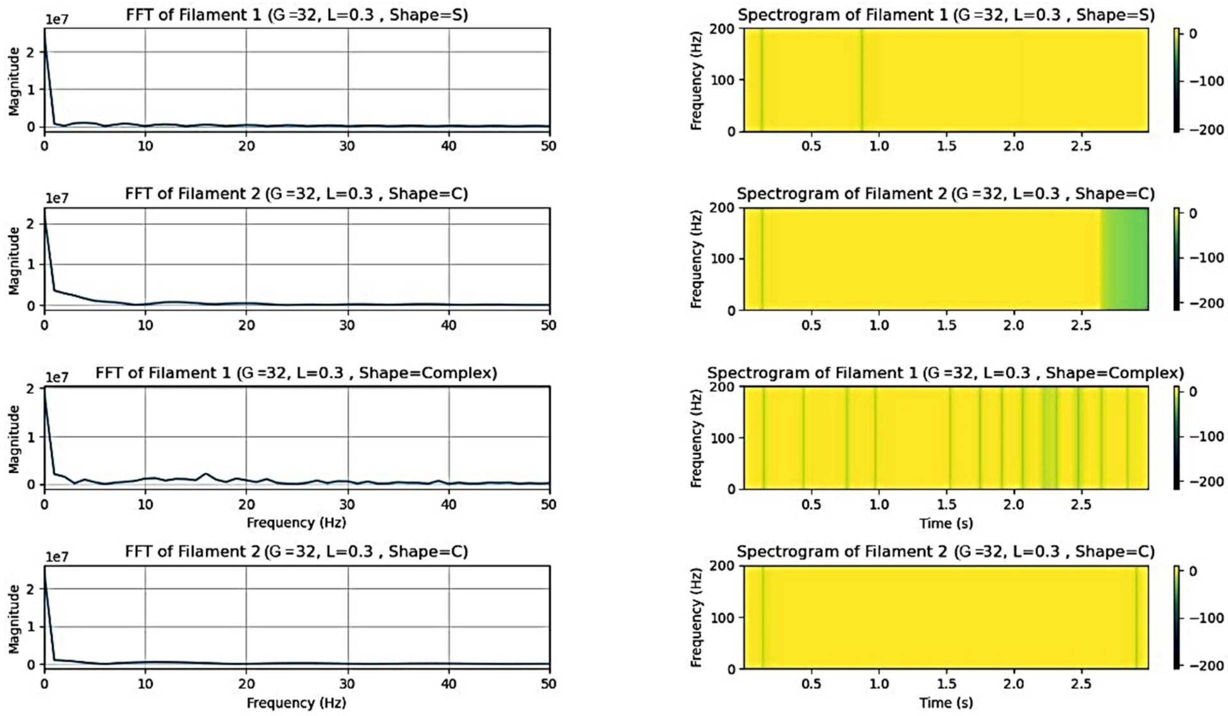

Fig. 17. FFT of filament deformation and spectrogram plot for F1 and F2 in order of shape formation for G = 32 and L = 0.3.

3.2. Machine Learning model predictions

A Machine Learning (ML) classifier such as Naive Bayes, SVM, K-nearest neighbor (KNN), Decision tree, and artificial neural network (ANN) are used to predict orbital regimes of filaments F1 and F2 in shear flow for various parameters. Let us examine each ML model used in this study.

The Naïve Bayes classifier [30] based on Bayes theorem is a classical probabilistic model known for its effectiveness in supervised learning. Its training process is based on the accuracy of the probabilistic model used. Notably, a class qualifies as an optimal classifier when some given feature shows no interdependence. Despite its simplicity, Bayes has proven to be highly successful in a variety of domains. This classifier operates based on Bayes' theorem, which calculates the probability of an event occurring given the probability of another event that has already occurred. Support Vector Machine (SVM) [31] works in a space, with dimensions by finding the hyper plane to accurately separate data points into different categories. The k-Nearest Neighbors (kNN) [32] algorithm is a non-parametric, instance-based learning algorithm that can be used for both classification and regression. The central idea behind kNN is that similar data points tend to exhibit similar behavior. The decision tree algorithm [33] commences with a feature set and proceeds to construct a decision tree structure for the classification of new instances. Each internal node within the decision tree encompasses a test, dictating the subsequent branch to be followed based on the test's outcome. At each stage of tree construction, the decision tree algorithm selects attributes that effectively partition the sample set into subsets enriched with distinct classes. The criterion for attribute selection hinges on normalized information gain, which serves to quantify the entropy disparity. Subsequently, the algorithm recursively partitions the subsets based on the chosen attributes. The construction of artificial neural networks (ANNs) [34] is inspired by the structure and function of biological neural networks. ANNs consist of interconnected nodes, or neurons, arranged in layers. These neurons process incoming signals and transmit output signals to other neurons within the network. Through algorithmic training, ANNs adapt the connections between neurons to perform specific tasks on example datasets, such as regression analysis, pattern recognition, and classification. This iterative training process enables ANNs to optimize their connections and effectively process input data, allowing them to accomplish various tasks with different levels of complexity and accuracy. Details regarding implementation of all the five algorithms in this study are shown on Fig. 18.

The development of a predictive model based on the results obtained from simulations is discussed. The application of five distinct Machine Learning classifiers: Naive Bayes, Support Vector Machine (SVM), K-nearest neighbor (KNN), Decision tree, and Artificial Neural Network (ANN) is elaborated upon. The length of the filament, its bending rigidity, and shear rate are taken as input features to the ML models. The models are tailored to categorize the orbit patterns of filaments in two dimensions. A comparative analysis is carried out on a similar platform using identical datasets across five different classifiers. The complete dataset is divided into two sets: training data and testing data. Eighty percent of the simulation data is selected randomly for training, and the remaining twenty percent is allocated for testing. To avoid overfitting data, classifier is evaluated using 10-fold cross-validation [35] for each model, where the data is divided into ten parts. In each fold, nine parts are used for training, and the remaining part are used for testing. This process is repeated ten times, with each part being used once for testing.

The performance of all the classifiers is evaluated using the formula given in Eq. (25) to Eq. (28):

$$\text{Accuracy} = \frac{TP + TN}{TP + TN + FP + FN} \tag{25}$$

$$\text{Recall} = \frac{TP}{TP + FN} \tag{26}$$

$$\text{Precision} = \frac{TP}{TP + FP} \tag{27}$$

$$\text{F1score} = 2 \times \frac{\text{Precision} \times \text{Recall}}{\text{Precision} + \text{Recall}} \tag{28}$$

where, the terms used in Eq. (25) to (28) are true positive (TP), true negative (TN), false positive (FP), and false negative (FN).

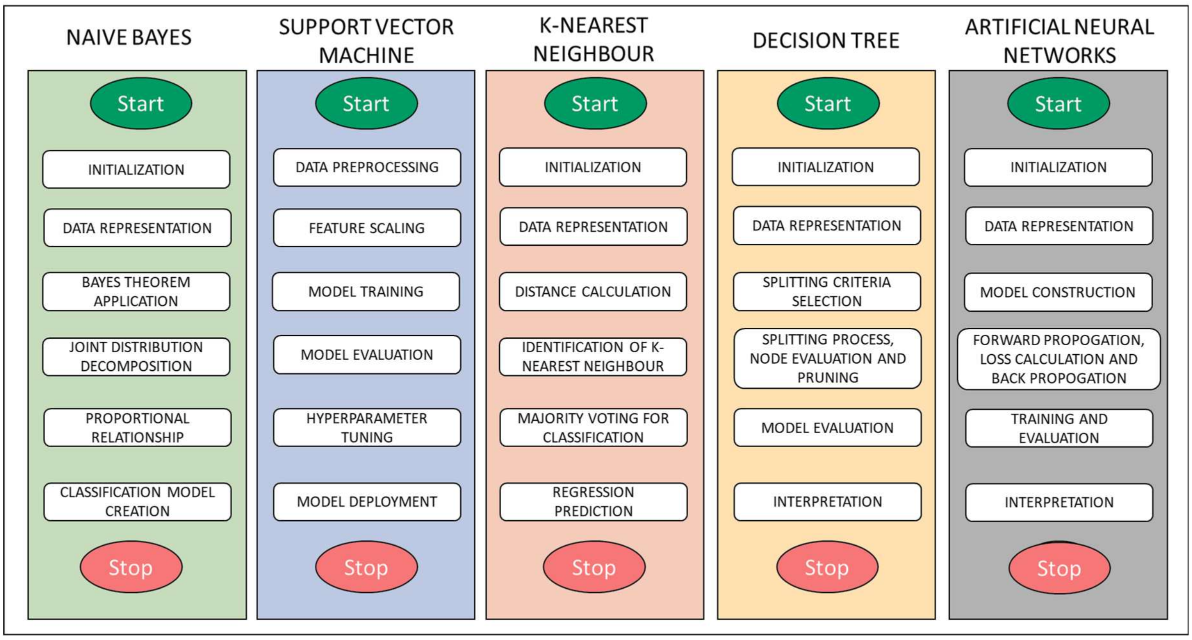

Fig. 18. Step-by-step implementation of various algorithms used for prediction of filament orbits.

Fig. 19. Average classification accuracies for F1 (blue) and F2 (orange) using five ML models.

PREDICTED CLASS \ ACTUAL CLASS	R	S	C	COMPLEX
R	15	4	0	0
S	1	30	7	0
C	0	0	34	8
COMPLEX	0	0	0	45

Fig. 20. Confusion matrix for F1 using KNN (Accuracy = 86.11%).

Figure 19 shows the accuracies obtained for F1 and F2 using Naive Bayes, Support Vector Machine (SVM), K-nearest neighbor (KNN), Decision tree, and Artificial Neural Network (ANN) classifiers. For F1, the classification accuracies are 58.33%, 46.53%, 86.11%, 81.94%, and 70.13%, respectively. The accuracy obtained for F2 are 47.92%, 43.05%, 88.89%, 75.69%, and 59.72%, respectively. These results highlight KNN as an efficient and accurate method for classifying the orbital regime of filaments under shear flow conditions with diverse parameters.

In configuring the KNN classifier for orbit class prediction, the input features: filament length, bending rigidity, and shear rate were normalized to the [0, 1] range to ensure uniform feature scaling and prevent any single feature from disproportionately influencing the Euclidean distance metric. This preprocessing step was crucial to maintain feature parity in the distance calculations, thereby ensuring that each parameter contributed equally to the classification decision. To determine the optimal number of neighbors (k), a tuning analysis was performed with k = 1, 2, and 3. The analysis revealed that k = 2 yielded the highest classification accuracy—86.11% for F1 and 88.89% for F2. The performance with k = 1 was slightly lower, achieving 84.72% for F1 and 87.5% for F2. However, a further increase to k = 3 led to a significant reduction in accuracy, with F1 at 77.77% and F2 at 79.86%. This behavior is consistent with typical patterns observed in small-to-moderate-sized datasets, where smaller k-values better capture local decision boundaries, while larger k-values tend to oversmooth the classification surface. Thus, the chosen configuration (k = 2) strikes an optimal balance between preserving local data structure and maintaining generalization capability for the orbit classification task.

Based on the provided performance metrics (Table 2), the K-Nearest Neighbors (KNN) prediction for F2 emerges as the most effective model, achieving the highest scores across all evaluated criteria, i.e., Precision (0.878), Recall (0.875), F1 Score (0.875), and ROC Area (0.929). This indicates that KNN of F2 not only accurately identifies positive instances but also maintains a strong balance between precision and recall, making it highly reliable overall. Additionally, KNN predictions of F1 demonstrate robust performance as well, particularly excelling in Precision (0.864) and Recall (0.861), though it slightly trails behind its F2 counterpart.

Artificial Neural Networks (ANN) shows commendable results, with predictions for F1 achieving a Precision of 0.700, Recall of 0.701, F1 Score of 0.678, and an impressive ROC Area of 0.895. ANN classification for F2 maintains solid performance, though it is marginally lower in Precision and F1 Score compared to F1. On the other hand, Support Vector Machines (SVM) and Naïve Bayes exhibit comparatively weaker performance, particularly in Precision and F1 Scores, where both predictions for F1 and F2 fall behind the other models. Decision Trees also perform well, with F1 achieving high scores in Precision (0.819), Recall (0.819), F1 Score (0.818), and ROC Area (0.903), while F2 shows slightly reduced performance. Overall, KNN predictions for F2 stands out as the best-performing model, with ANN and Decision Trees as viable alternatives, whereas SVM and Naïve Bayes may require further optimization for improved effectiveness in this application.

Finally, the confusion matrix, in Fig. 20 and Fig. 21 for F1 and F2, respectively, presents the classification errors encountered by the KNN classifier across different shapes. These misclassifications likely stem from the inherent overlap in patterns associated with each shape category. This underscores the imperative of exploring new feature sets capable of enhancing discrimination between shapes, thus facilitating more accurate classification outcomes.

Table 2. Performance comparison of various machine learning models across Precision, Recall, F1 Score, and ROC Area Metrics

	Naive Bayes		SVM		ANN		KNN		Decision Tree	
	F1	F2	F1	F2	F1	F2	F1	F2	F1	F2
Precision	0.640	0.511	0.560	0.398	0.700	0.601	0.864	0.878	0.819	0.754
Recall	0.583	0.479	0.465	0.431	0.701	0.597	0.861	0.875	0.819	0.757
F1 score	0.545	0.433	0.475	0.354	0.678	0.596	0.859	0.875	0.818	0.755
ROC Area	0.844	0.763	0.619	0.567	0.895	0.802	0.915	0.929	0.903	0.866

		ACTUAL CLASS			
		R	***S***	***C***	***COMPLEX***
PREDICTED CLASS	***R***	18	1	0	0
	S	3	32	4	0
	C	0	3	44	5
	COMPLEX	0	0	1	34

Fig. 21. Confusion matrix for F2 using KNN (Accuracy = 88.89%).

4. Conclusion

A two-dimensional numerical simulation of two filaments placed side-by-side in shear flow is performed using formally second-order immersed boundary method. The categorization of fiber deformations of both the filaments into various orbit classes such as Rigid, Springy, C-shape, S-shape and Complex shapes is done with the help of parametric studies involving various parameters like filament lengths, shear rate and bending rigidities. The demarcation of filaments dynamic behaviour can be approximated to a flow-filament offset ratio φ. Results indicate that at higher shear rates and high filament lengths, there is marginal effect of first filament on the surrounding hydrodynamic forces and the deformation of second filament is not influenced by first filament. For the first filament (F1) to exert any influence on the second filament (F2) deformation, the filament length should be medium ($L \approx$ 0.2) and high shear rate ($G \approx$ 32). When analysing filament deformations using spectrogram data, it is found that F1 absorbs hydrodynamic forces resulting in multiple energy band formations whereas the second filament (F2) receives lower levels of fluid forces, thus leading to retarded motion and with large band gaps. The observations from this study will help in designing microfluidic devices for cell/particle sorting where multiple flexible filaments can be utilized and particles of various sizes can be sorted. Finally, development of a predictive model based on the results obtained from simulations is provided by five distinct Machine Learning classifiers: Naive Bayes, Support Vector Machine (SVM), K-nearest neighbor (KNN), Decision tree, and Artificial Neural Network (ANN). In order to avoid overfitting of data, classifier is evaluated using 10-fold cross-validation for each model. Performance test results highlight K-Nearest Neighbors (KNN) as an efficient and accurate method for classifying the orbital regime of filaments under shear flow conditions. The KNN prediction for F2 emerges as the most effective model, achieving the highest scores across all evaluated criteria, i.e., Precision (0.878), Recall (0.875), F1 Score (0.875), and ROC Area (0.929). Overall, KNN predictions for F2 stands out as the best-performing model, with ANN and Decision Trees as viable alternatives, whereas SVM and Naïve Bayes may require further optimization for improved effectiveness in this application.

Author Contributions

M. Kanchan contributed to the conceptualization, methodology, investigation, validation, supervision, writing-original draft, writing-editing, review. R. Maniyeri contributed to supervision, writing-editing, review. O.S. Powar conducted the data processing, Machine learning algorithm, validation, writing-editing. The manuscript was written through the contribution of all authors. All authors discussed the results, reviewed, and approved the final version of the manuscript.

Acknowledgments

The authors would like to acknowledge the support provided for materials and computational facility by Department of Mechanical and Industrial Engineering, Manipal Institute of Technology, Manipal Academy of Higher Education, Manipal.

Conflict of Interest

The authors declared no potential conflicts of interest concerning the research, authorship, and publication of this article.

Funding

The authors received no financial support for the research of this article.

Data Availability Statements

The datasets generated and/or analyzed during the current study are available from the corresponding author on reasonable request.

Nomenclature

H_c^*	Channel height [cm]	μ	Fluid viscosity [g/(cm.s)]
L_c^*	Channel width [cm]	G	Shear rate (1/s)
ρ	Fluid density [g/cm^3]	L^*	Filament length [m]
$\boldsymbol{u}$	Fluid velocity [m/s]	U	Filament velocity [m/s]
$\boldsymbol{f}$	Eulerian forcing term [N/m^2]	F	Lagrangian forcing term [N/m^2]
$\boldsymbol{x}(\boldsymbol{x},\boldsymbol{y})$	Eulerian coordinates	$\boldsymbol{X}(s,t)$	Lagrangian coordinates

References

[1] Nguyen, H., Fauci, L., Hydrodynamics of diatom chains and semiflexible fibres, *Journal of The Royal Society Interface*, 11(96), 2014, 20140314.
[2] Bustamante, C., Bryant, Z., Smith, S.B., Ten years of tension: single-molecule DNA mechanics, *Nature*, 421(6921), 2003, 423-427.
[3] Peters, J.P., Yelgaonkar, S.P., Srivatsan, S.G., Tor, Y., Maher III, L.J., Mechanical properties of DNA-like polymers, *Nucleic Acids Research*, 41(22), 2013, 10593-10604.
[4] Gardel, M.L., Synthetic polymers with biological rigidity, *Nature*, 493(7434), 2013, 619.
[5] Jeffery, G.B., The motion of ellipsoidal particles immersed in a viscous fluid, *Proceedings of the Royal Society of London. Series A*, 102(715), 1922, 161-179.
[6] Anczurowski, E., Mason, S.G., The kinetics of flowing dispersions: III. Equilibrium orientations of rods and discs (experimental), *Journal of Colloid and Interface Science*, 23(4), 1967, 533-546.
[7] Forgacs, O.L., Mason, S.G., Particle motions in sheared suspensions: X. Orbits of flexible threadlike particles, *Journal of Colloid Science*, 14(5), 1959, 473-491.
[8] Kock, I., Edler, T., Mayr, S.G., Growth behavior and intrinsic properties of vapor-deposited iron palladium thin films, *Journal of Applied Physics*, 103(4), 2008.
[9] Ross, R.F., Klingenberg, D.J., Dynamic simulation of flexible fibers composed of linked rigid bodies, *The Journal of Chemical Physics*, 106(7), 1997, 2949-2960.
[10] Shelley, M.J., Ueda, T., The Stokesian hydrodynamics of flexing, stretching filaments, *Physica D: Nonlinear Phenomena*, 146(1-4), 2000, 221-245.
[11] Tornberg, A.K., Shelley, M.J., Simulating the dynamics and interactions of flexible fibers in Stokes flows, *Journal of Computational Physics*, 196(1), 2004, 8-40.
[12] Jendrejack, R.M., Schwartz, D.C., De Pablo, J.J., Graham, M.D., Shear-induced migration in flowing polymer solutions: Simulation of long-chain DNA in microchannels, *The Journal of Chemical Physics*, 120(5), 2004, 2513-2529.
[13] Lindström, S.B., Uesaka, T., Simulation of the motion of flexible fibers in viscous fluid flow, *Physics of Fluids*, 19(11), 2007, 113307.
[14] Lindström, S.B., Uesaka, T., A numerical investigation of the rheology of sheared fiber suspensions, *Physics of Fluids*, 21(8), 2009, 083301.
[15] Bouzarth, E.L., Layton, A.T., Young, Y.N., Modeling a semi-flexible filament in cellular Stokes flow using regularized Stokeslets, *International Journal for Numerical Methods in Biomedical Engineering*, 27(12), 2011, 2021-2034.
[16] Słowicka, A.M., Wajnryb, E., Ekiel-Jezewska, M.L., Dynamics of flexible fibers in shear flow, *The Journal of Chemical Physics*, 143(12), 2015, 124904.
[17] Peskin, C.S., The immersed boundary method, *Acta Numerica*, 11, 2002, 479-517.
[18] Stockie, J.M., Green, S.I., Simulating the motion of flexible pulp fibres using the immersed boundary method, *Journal of Computational Physics*, 147(1), 1998, 147-165.
[19] Wiens, J.K., Stockie, J.M., Simulating flexible fiber suspensions using a scalable immersed boundary algorithm, *Computer Methods in Applied Mechanics and Engineering*, 290, 2015, 1-18.
[20] Kanchan, M., Maniyeri, R., Numerical analysis of the buckling and recuperation dynamics of flexible filament using an immersed boundary framework, *International Journal of Heat and Fluid Flow*, 77, 2019, 256-277.
[21] Miyanawala, T.P., Jaiman, R.K., A hybrid data-driven deep learning technique for fluid-structure interaction, *International Conference on Offshore Mechanics and Arctic Engineering*, Glasgow, Scotland, UK, 58776, V002T08A004, 2019.
[22] Koh, J.B.Y., Shen, X., Marcos, Supervised learning to predict sperm sorting by magnetophoresis, *Magnetochemistry*, 4(3), 2018, 31.
[23] Fayed, M., Elhadary, M., Abderrahmane, H.A., Zakher, B.N., The ability of forecasting flapping frequency of flexible filament by artificial neural network, *Alexandria Engineering Journal*, 58(4), 2019, 1367-1374.
[24] Kanchan, M., Maniyeri, R., Numerical simulation and prediction model development of multiple flexible filaments in viscous shear flow using immersed boundary method and artificial neural network techniques, *Fluid Dynamics Research*, 52(4), 2020, 045507.
[25] Ntetsika, M., Papadopoulos, P., Numerical simulation and predictive modeling of an inextensible filament in two-dimensional viscous shear flow using the Immersed Boundary/Coarse-Graining Method and Artificial Neural Networks, *Computer Methods in Applied Mechanics and Engineering*, 401, 2022, 115589.
[26] Kanchan, M., Maniyeri, R., Fluid–structure interaction study and flowrate prediction past a flexible membrane using immersed boundary method and artificial neural network techniques, *Journal of Fluids Engineering*, 142(5), 2020, 051501.
[27] Kanchan, M., Lewis, D., Varma, A., Fluid-induced deformation of elastic plate mounted vertically in viscous flow and oscillation frequency prediction using artificial neural networks, *Ocean Engineering*, 296, 2024, 116920.
[28] Kanchan, M., Maniyeri, R., Numerical simulation of buckling and asymmetric behavior of flexible filament using temporal second-order immersed boundary method, *International Journal of Numerical Methods for Heat & Fluid Flow*, 30(3), 2020, 1047-1095.
[29] Hayase, T., Humphrey, J.A.C., Greif, R., A consistently formulated QUICK scheme for fast and stable convergence using finite-volume iterative calculation procedures, *Journal of Computational Physics*, 98(1), 1992, 108-118.
[30] Bayes, T., Naive Bayes classifier, *Article Sources and Contributors*, 1968, 1-9.
[31] Hearst, M.A., Dumais, S.T., Osuna, E., Platt, J., Scholkopf, B., Support vector machines, *IEEE Intelligent Systems and Their Applications*, 13(4), 1998, 18-28.
[32] Peterson, L.E., K-nearest neighbor, *Scholarpedia*, 4(2), 2009, 1883.
[33] Song, Y.Y., Ying, L.U., Decision tree methods: applications for classification and prediction, *Shanghai Archives of Psychiatry*, 27(2), 2015, 130.
[34] Haykin, S., *Neural Networks: A Comprehensive Foundation*, Prentice Hall PTR, New Jersey, 1998.
[35] Hastie, T., *The Elements of Statistical Learning: Data Mining, Inference, and Prediction*, Springer, New York, 2009.

ORCID iD

Mithun Kanchan https://orcid.org/0000-0002-8694-770X
Ranjith Maniyeri https://orcid.org/0000-0001-5997-473X
Omkar S. Powar https://orcid.org/0000-0003-4646-8787

How to cite this article: Kanchan M., Maniyeri R., Powar O.S. Numerical Analysis of Two Side-by-side Flexible Filaments in Shear Flow and Orbit Class Prediction using Immersed Boundary Method and Machine Learning Techniques, *J. Appl. Comput. Mech.*, 12(1), 2026, 238-254. https://doi.org/10.22055/jacm.2025.48275.5112